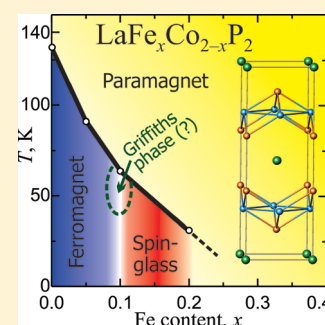


Spin-Glass Behavior in $\text{LaFe}_x\text{Co}_{2-x}\text{P}_2$ Solid Solutions: Interplay Between Magnetic Properties and Crystal and Electronic StructuresKirill Kovnir,^{†,‡} V. Ovidiu Garlea,[‡] Corey M. Thompson,[†] H. D. Zhou,[§] William M. Reiff,^{||,§} Andrew Ozarowski,[§] and Michael Shatruk^{*,†,§}[†]Department of Chemistry and Biochemistry, Florida State University, Tallahassee, Florida 32306, United States[‡]Neutron Scattering Science Division, Oak Ridge National Laboratory, Oak Ridge, Tennessee 37831, United States[§]National High Magnetic Field Laboratory, Florida State University, Tallahassee, Florida 32310, United States^{||}Department of Chemistry and Chemical Biology, Northeastern University, Boston, Massachusetts 02115, United States

Supporting Information

ABSTRACT: To explore the evolution of magnetic properties from ferromagnetic LaCo_2P_2 to paramagnetic LaFe_2P_2 (both of ThCr_2Si_2 structure type) a series of mixed composition $\text{LaFe}_x\text{Co}_{2-x}\text{P}_2$ ($x \leq 0.5$) has been comprehensively investigated by means of single-crystal and powder X-ray and neutron diffraction, magnetization and heat capacity measurements, Mössbauer spectroscopy, and electronic band structure calculations. The Curie temperature decreases from 132 K in LaCo_2P_2 to 91 K in $\text{LaFe}_{0.05}\text{Co}_{1.95}\text{P}_2$. The ferromagnetic ordering is suppressed at higher Fe content. $\text{LaFe}_{0.1}\text{Co}_{1.9}\text{P}_2$ and $\text{LaFe}_{0.2}\text{Co}_{1.8}\text{P}_2$ demonstrate spin-glass-like behavior, which was also confirmed by the absence of characteristic features of long-range magnetic ordering, namely, a λ -type anomaly in the heat capacity, a hyperfine splitting in the Mössbauer spectrum, and magnetic reflections in the neutron diffraction pattern. Finally, both $\text{LaFe}_{0.3}\text{Co}_{1.7}\text{P}_2$ and $\text{LaFe}_{0.5}\text{Co}_{1.5}\text{P}_2$ exhibit paramagnetic behavior down to 1.8 K. The unit cell parameters of the mixed compounds do not follow the Vegard behavior as the increase in the Fe content results in the decrease of average M–M distances (M = Fe, Co). Quantum-chemical calculations and crystal orbital Hamiltonian population analysis reveal that upon aliovalent (nonisoelectronic) substitution of Fe for Co the antibonding character of M–M interactions is reduced while the Fermi level is shifted below the DOS peak in the 3d metal subband. As the result, at higher Fe content the Stoner criterion is not satisfied and no magnetic ordering is observed.



INTRODUCTION

Fe-containing pnictides that belong to the ThCr_2Si_2 structure type have been a focus of attention of the inorganic and materials science community since the recent discovery of superconductivity in doped AFe_2As_2 (A = Ca, Sr, Ba, Eu).¹ The parent ternary AFe_2As_2 phases are not superconductors, but proper doping into either metal or pnictogen sublattice leads to emergence of superconducting properties.² In turn, recent studies have shown that Co-containing analogues exhibit very rich magnetic behavior, including field- and temperature-induced metamagnetism,³ magnetic pole reversal,³ and quantum phase transitions.⁴

Ternary phosphides RCo_2P_2 (R = rare-earth metal) deserve special consideration among the ThCr_2Si_2 -type compounds as they appear to be on the verge of magnetic instability. Indeed, LaCo_2P_2 is characterized by ferromagnetic ordering of Co magnetic moments at 132 K,^{3,5} while the other representatives of this family (R = Ce, Pr, Nd, Sm) exhibit antiferromagnetic ordering of Co moments above 300 K.⁶ In EuCo_2P_2 , the Co sublattice does not show magnetic ordering under ambient pressure but exhibits an antiferromagnetic transition at 260 K under pressure exceeding 3.1 GPa, which was explained by the pressure-induced change in the oxidation state of Eu from +2 to +3.⁷ It also was noted that the antiferromagnetically ordered

phases in this series are always characterized by a rather short P–P separation (~ 2.5 Å) between the $[\text{Co}_2\text{P}_2]$ layers of the crystal structure (Figure 1),⁸ and therefore, the antiferromagnetic order might be attributed to the collapse of the structure along the c axis.

Recently, we have shown that not only structural but also electronic factors play a crucial role in defining the magnetic behavior of these materials. Thus, the Curie temperature of LaCo_2P_2 was raised to as high as 268 K in $\text{La}_{1-x}\text{Pr}_x\text{Co}_2\text{P}_2$ by increasing the intralayer Co–Co distances, even though the interlayer P–P separation decreased to 2.68 Å³ (compare to 3.16 Å in LaCo_2P_2).⁸ Furthermore, antiferromagnetism in PrCo_2P_2 and ferromagnetism in $\text{Pr}_{0.8}\text{Eu}_{0.2}\text{Co}_2\text{P}_2$ were observed at essentially the same interlayer P–P separation (~ 2.57 Å) in both structures.⁹

Obviously, the changes in the electronic structure have important ramifications on the magnetic properties of these materials. Thus, in contrast to the LaCo_2P_2 , which exhibits ferromagnetic ordering at 132 K, LaFe_2P_2 behaves as a classical paramagnet with a Curie–Weiss-like temperature dependence

Received: June 21, 2011

Published: September 15, 2011

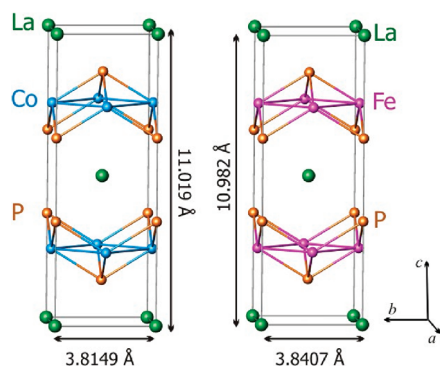


Figure 1. Crystal structures of LaCo_2P_2 and LaFe_2P_2 .

of magnetic susceptibility from 2 to 300 K.⁵ To understand how the magnetic behavior of LaCo_2P_2 evolves upon substitution of Fe for Co, we undertook a comprehensive study of mixed phases $\text{LaFe}_x\text{Co}_{2-x}\text{P}_2$ ($x \leq 0.5$) by means of magnetization and heat capacity measurements, single-crystal X-ray diffraction, variable-temperature powder X-ray and neutron diffraction, Mössbauer spectroscopy, and quantum-chemical calculations. Herein, we report the results of this investigation and elaborate on the change from ferromagnetic to spin-glass-like to paramagnetic behavior with increasing Fe content in $\text{LaFe}_x\text{Co}_{2-x}\text{P}_2$. We especially stress the importance of electronic factors in the observed modification of structural and magnetic properties.

EXPERIMENTAL SECTION

Starting Materials. Finely dispersed powders of lanthanum (99.9%) and red phosphorus (99.999%) as well as tin shots (99.99%) were obtained from Alfa Aesar and used as received. Cobalt and iron powders (Alfa Aesar, 99.5%) were additionally purified by heating for 5 h in a flow of H_2 gas at 775 K. All manipulations during sample preparation were carried out in an argon-filled drybox (content of $\text{O}_2 < 1$ ppm). Isotope-pure ^{57}Fe foil was obtained from Cyclotron Instruments, Mainz, Germany, and used for the synthesis of the isotopically enriched sample for Mössbauer spectroscopy. ^{57}Fe foil was dissolved in dilute nitric acid, and iron hydroxide was precipitated by adding excess aqueous ammonia solution. Reduction of the precipitate in a flow of H_2 gas at 1073 K for 7 h resulted in a phase-pure ^{57}Fe powder.

Synthesis. Preparation of lanthanum iron–cobalt phosphides, $\text{LaFe}_x\text{Co}_{2-x}\text{P}_2$ ($x = 0, 0.05, 0.1, 0.2, 0.3, 0.5,$ and 1), followed the tin flux synthetic procedure described in the literature for LaCo_2P_2 and LaFe_2P_2 .⁶ The starting materials were mixed in a La:Fe:Co:P:Sn = 1.6: x :($2-x$):2:30 ratio (total mass = 5 g) in 10 mm i.d. silica tubes, which were sealed under vacuum ($<10^{-2}$ mbar). The mixtures were annealed at 1155 K for 10 days, cooled down to 875 K at 10 K/min, and quenched into water. Tin flux was removed by soaking the samples in dilute HCl (1:1 v/v). At this point, X-ray-quality single crystals were selected from the samples. The phase purity of bulk products obtained by the described synthetic procedure was checked by powder X-ray diffraction. A $\text{LaFe}_{0.1}\text{Co}_{1.9}\text{P}_2$ sample for neutron powder diffraction experiments was prepared by scaling up the total sample weight to 50 g and using a larger tube with 25 mm i.d.

Physical Measurements. Elemental analysis of select single crystals was carried out on a JEOL 5900 scanning electron microscope with an energy-dispersive X-ray (EDX) microanalysis. Magnetic measurements were performed on polycrystalline samples with a Quantum Design SQUID magnetometer MPMS-XL. Direct current (dc) magnetic susceptibility measurements were carried out in various applied fields from 0.0005 to 0.4 T and in the 1.8–300 K temperature range.

Isothermal dependences of magnetization were measured with the magnetic field varying from 0 to 7 T. Alternating current (ac) magnetic susceptibility was measured in the 1.8–200 K range at frequencies of 1, 10, 100, and 1000 Hz with an ac field amplitude of 0.0003 T. The heat capacity was measured with a Quantum Design Physical Property Measurement System in the temperature range of 1.8–150 K and at zero applied field.

Powder X-ray Diffraction. Room-temperature powder X-ray diffraction was performed on an original setup based on a Huber Guinier camera 670 with an imaging plate using $\text{Cu K}\alpha_1$ radiation ($\lambda = 1.54060$ Å) and Ge as an internal standard. Standardless variable-temperature powder X-ray diffraction data were collected in the temperature range of 10–300 K by employing a closed-cycle He refrigeration system. Unit cell parameters were calculated by refinement of a set of 12 reflections common to all samples. The WinCSD software package was used for least-squares refinement of the unit cell parameters.¹⁰

Single-Crystal X-ray Diffraction. Room-temperature experiments were carried out using a Bruker AXS SMART diffractometer with an APEX-II CCD detector. The data sets were recorded as ω scans at 0.3° step width and integrated with the Bruker SAINT software package.¹¹ All data sets were indexed in the tetragonal body-centered unit cell. The only systematic extinctions observed corresponded to the I -centered lattice. Analytical adsorption correction was applied using face indexing of the crystal. Solution and refinement of the crystal structures were carried out using the SHELX suite of programs.¹² The structures were solved in the $I4/mmm$ space group (No. 139), and the final refinement was performed with anisotropic atomic displacement parameters (ADPs) for all atoms. Refinement of Fe and Co site occupancy factors (s.o.f.s) was not possible due to the very close X-ray scattering factors of these neighboring elements. Since the nominal Fe/Co ratio agreed well with the results of EDX microanalysis, the Fe and Co s.o.f.s in the 4d ($0, 1/2, 1/4$) position were fixed to the nominal composition, with a constraint of equal ADPs. The summary of pertinent information relating to unit cell parameters, data collection, and refinements is provided in Table 1.

Mössbauer Spectroscopy. Mössbauer spectra were determined using a conventional constant acceleration spectrometer operated in multichannel scaling mode. The gamma-ray source consisted of ~ 60 mCi of ^{57}Co in a rhodium metal matrix that was maintained at ambient temperature. The pulse height analysis spectrum for the $^{57}\text{Co}/\text{Rh}$ 14.4 keV gamma-ray source was determined using a Reuter–Stokes gas proportional counter filled to 1 atm with a Kr/CO_2 gas mixture. ^{57}Fe Mössbauer spectra were collected using the same source and detector. The spectrometer was calibrated using a $6 \mu\text{m}$ thick natural abundance iron foil for which the line widths of the innermost pair of $\Delta M_1 = \pm 1$ transitions of the corresponding Zeeman pattern were reproducibly found to be 0.214 mm/s. The $\text{LaFe}_{0.1}\text{Co}_{1.9}\text{P}_2$ isomer shifts were determined relative to the center of the foregoing $6 \mu\text{m}$ Fe foil absorber. To improve the signal-to-noise ratio, an iron-57 isotopically enriched sample $\text{La}^{57}\text{Fe}_{0.1}\text{Co}_{1.9}\text{P}_2$ was also prepared and investigated. Both natural and isotope-enriched samples exhibit similar spectra. Therefore, only the data obtained for $\text{La}^{57}\text{Fe}_{0.1}\text{Co}_{1.9}\text{P}_2$ are discussed below. The Voigt function was used for theoretical spectrum fitting in order to account for both the finite thickness effect (Lorentzian broadening) and the intrinsic Fe-atom coordination in the compound investigated (Gaussian broadening). To avoid possible correlations between the Gaussian and the Lorentzian full widths at half-maximum, the latter was fixed to 0.375 mm/s, a value obtained by fitting the room-temperature spectrum. The Gaussian quadrupole splitting is reported below.

Neutron Powder Diffraction. Neutron powder diffraction experiments on $\text{LaFe}_{0.1}\text{Co}_{1.9}\text{P}_2$ were carried out using the HB-2A high-resolution neutron powder diffractometer at the High Flux Isotope Reactor at Oak Ridge National Laboratory. Two different wavelengths, $\lambda = 1.536$ and 2.410 Å, were provided by vertically focusing Ge (115) and (113) monochromators, respectively. The data were collected by

Table 1. Data Collection and Structure Refinement Parameters for $\text{LaFe}_x\text{Co}_{2-x}\text{P}_2$ ^a

nominal composition	$\text{LaFe}_{0.05}\text{Co}_{1.95}\text{P}_2$	$\text{LaFe}_{0.1}\text{Co}_{1.9}\text{P}_2$	$\text{LaFe}_{0.2}\text{Co}_{1.8}\text{P}_2$	$\text{LaFe}_{0.3}\text{Co}_{1.7}\text{P}_2$	$\text{LaFe}_{0.5}\text{Co}_{1.5}\text{P}_2$
<i>x</i> , Fe content from EDX	0.08(2)	0.11(1)	0.20(1)	0.34(2)	0.51(1)
space group	<i>I4/mmm</i> (No. 139)	<i>I4/mmm</i> (No. 139)	<i>I4/mmm</i> (No. 139)	<i>I4/mmm</i> (No. 139)	<i>I4/mmm</i> (No. 139)
unit cell, Å	<i>a</i> = 3.8083(2) <i>c</i> = 11.0562(5)	<i>a</i> = 3.8094(1) <i>c</i> = 11.0879(3)	<i>a</i> = 3.8060(1) <i>c</i> = 11.1125(3)	<i>a</i> = 3.7994 (1) <i>c</i> = 11.1598(3)	<i>a</i> = 3.8060(1) <i>c</i> = 11.2211(3)
<i>V</i> , Å ³	160.35(1)	160.902(7)	160.972(7)	161.097(7)	162.545(7)
<i>Z</i>	2	2	2	2	2
ρ_{calc} , g cm ⁻³	6.598	6.572	6.563	6.551	6.480
μ , mm ⁻¹	23.965	23.850	23.776	23.693	23.354
λ , Å	Mo <i>K</i> α , 0.71073	Mo <i>K</i> α , 0.71073	Mo <i>K</i> α , 0.71073	Mo <i>K</i> α , 0.71073	Mo <i>K</i> α , 0.71073
temp.	293 K	293 K	293 K	293 K	293 K
$2\theta_{\text{max}}$	80	80	80	80	80
reflins collected	1266	1116	1069	1051	1135
R_{int}	0.017	0.026	0.017	0.016	0.016
unique reflns	174	178	170	179	180
params refined	9	9	9	9	9
R_1 , wR_2 [$F_o > 4\sigma(F_o)$]	0.012, 0.030	0.018, 0.041	0.013, 0.034	0.013, 0.034	0.018, 0.045
diff. peak and hole, e/Å ³	0.91, -1.52	1.42, -2.56	1.02, -1.00	1.48, -1.21	2.14, -1.08
goodness-of-fit	1.28	1.11	1.20	1.22	1.33
CSD number	423087	423086	423085	423084	423083

^a Further details of the crystal structure determination may be obtained from Fachinformationszentrum Karlsruhe, D-76344 Eggenstein-Leopoldshafen, Germany, on quoting the depository CSD numbers.

scanning the detector array consisting of 44 ³He tubes in two segments to cover the total 2θ range of 4–150° in steps of 0.05°. Overlapping detectors for the given step served to average the counting efficiency of each detector. More details about the HB-2A instrument and data collection strategies can be found in the original publication.¹³ Measurements were performed on a sample of ~3 g held in a cylindrical vanadium container in a top-loading closed-cycle refrigerator in the temperature range of 4–300 K.

Quantum-Chemical Calculations. Band structure calculations were performed with the tight binding-linear muffin tin orbitals-atomic sphere approximation (TB-LMTO-ASA) software package.¹⁴ The von Barth–Hedin exchange-correlation potential was employed for local density approximation (LDA) calculations.¹⁵ The radial scalar-relativistic Dirac equation was solved to obtain the partial waves. The structural parameters used (unit cell dimensions and atomic coordinates) were taken from the reported room-temperature crystal structures of LaCo_2P_2 and LaFe_2P_2 .⁶ No empty spheres had to be added. For LaCo_2P_2 and LaFe_2P_2 , the calculations were performed in the original unit cell and space group ($a_0 \times a_0 \times c_0$, *I4/mmm*) for a $28 \times 28 \times 28$ *k*-point mesh with 1639 irreducible *k* points. For LaFeCoP_2 and $\text{LaFe}_{0.5}\text{Co}_{1.5}\text{P}_2$, superstructures were constructed by starting from the original unit cell of LaCo_2P_2 and lowering the symmetry. LaFeCoP_2 : the original unit cell ($a_0 \times a_0 \times c_0$), space group *Pmmm*, a $42 \times 42 \times 14$ *k*-point mesh with 3872 irreducible *k* points. $\text{LaFe}_{0.5}\text{Co}_{1.5}\text{P}_2$: a supercell ($2a_0 \times 2a_0 \times c_0$), space group *Pmmm*, a $15 \times 15 \times 10$ *k*-point mesh with 384 irreducible *k* points. Integration over the Brillouin zone was carried out by the tetrahedron method.¹⁶ The basis set contained La(6s, 5d, 4f), Fe(4s, 4p, 3d), Co(4s, 4p, 3d), and P(3s, 3p) orbitals, with the La(6p) and P(3d) functions being downfolded.¹⁷

RESULTS AND DISCUSSION

Synthesis. As shown earlier by Jeitschko et al.,⁶ LaCo_2P_2 is resistant to a dilute (1:1 v/v) HCl solution while LaFe_2P_2 slowly dissolves under such conditions. In our experiments, we were able to synthesize phase-pure $\text{LaFe}_x\text{Co}_{2-x}\text{P}_2$ ($x = 0.05, 0.1, 0.2,$

Table 2. Magnetic Properties of $\text{LaFe}_x\text{Co}_{2-x}\text{P}_2$

Fe content, <i>x</i>	T_C , K	T_{SG} , K ^a	θ , K
0	132		135
0.05	91(2)		71(2)
0.10		59(3)	50(2)
0.20		31(2)	101(2)
0.30			116(2)
0.50			137(2)

^a T_{SG} = temperature of spin-glass magnetic transition.

and 0.3). The sample $\text{LaFe}_{0.5}\text{Co}_{1.5}\text{P}_2$ contains a minor admixture of CoP_2 , which was reported to be diamagnetic.¹⁸ EDX analysis reveals that the Fe/Co ratio in the obtained crystals agrees well with the nominal composition used for sample preparation (Table 1). Several areas of each crystal were examined, giving consistent results and not showing any signs of inhomogeneity. Therefore, in the following discussion, the nominal Fe content will be used. Powder X-ray diffraction analyses confirmed that all the samples are phase pure and crystallize in the ThCr_2Si_2 structure type. The unit cell volume increases with the increase in Fe content (see Figure 10 in the Crystal Structure section), which confirms the bulk substitution of Fe for Co and agrees with the EDX results.

It appears that increasing the Fe content results in a decreased stability against acid treatment, as samples with $x > 0.5$ were contaminated with phosphides M_2P ($\text{M} = \text{Co}, \text{Fe}$). Solid solutions $\text{Fe}_x\text{Co}_{2-x}\text{P}$ are known to exhibit magnetic ordering at high temperatures for $x > 0.5$,¹⁹ and therefore, the samples with high Fe content were not characterized further.

Magnetic Properties. Somewhat unconventionally, we begin with the description of magnetic properties, as the other parts of the paper will serve to support conclusions derived from the magnetic behavior observed. LaCo_2P_2 exhibits ferromagnetic

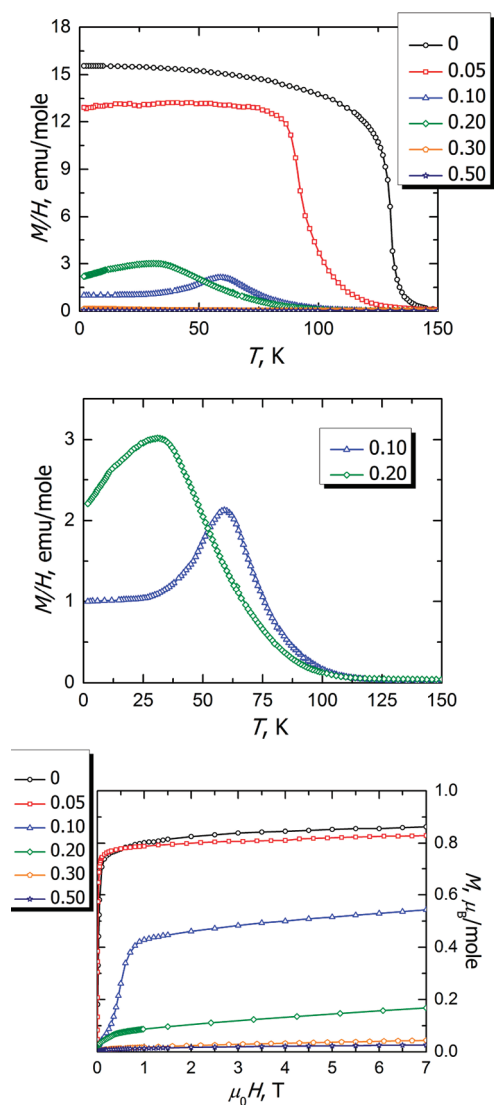


Figure 2. Magnetic properties of $\text{LaFe}_x\text{Co}_{2-x}\text{P}_2$. (Top) Temperature dependences of dc magnetic susceptibilities measured at 0.0005 T for the sample with $x = 0.2$ and at 0.001 T for all other samples. (Middle) Enlarged temperature dependences of susceptibility for the samples with $x = 0.10$ and 0.20 . (Bottom) Field dependences of magnetization at 1.8 K. The solid lines are guides for the eye.

ordering at $T_C = 132$ K, Table 2.³ Introduction of a small amount of iron ($x = 0.05$) decreases the ordering temperature to 91 K (Figure 2, top).²⁰ The samples with $x = 0.1$ and 0.2 exhibit a cusp in the temperature dependence of magnetic susceptibility at 59 and 31 K, respectively (Figure 2, middle). Finally, the samples with $x = 0.3$ and 0.5 exhibit no magnetic ordering down to 1.8 K. Fitting the high-temperature part of the curves to the Curie–Weiss law yields positive Weiss constants for all samples (Table 2), thus indicating ferromagnetic nearest-neighbor interactions in $\text{LaFe}_x\text{Co}_{2-x}\text{P}_2$. The isothermal field dependences of magnetization at 1.8 K show a substantial decrease in the total saturation moment with increasing Fe content (Figure 2, bottom).

Further examination of samples with $x = 0.1$ and 0.2 revealed divergence of field-cooled and zero-field-cooled magnetization curves (Figure S1, Supporting Information), suggesting possible

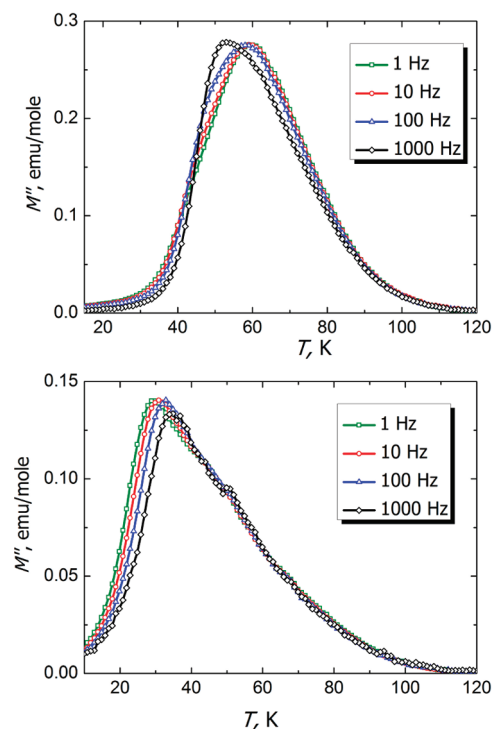


Figure 3. Temperature dependence of the imaginary part of ac magnetic susceptibilities of $\text{LaFe}_{0.1}\text{Co}_{1.9}\text{P}_2$ (top) and $\text{LaFe}_{0.2}\text{Co}_{1.8}\text{P}_2$ (bottom) in zero dc bias field.

spin-glass behavior. Indeed, ac magnetic susceptibility measurements showed the presence of frequency-dependent maxima in the imaginary part of magnetization for both samples (Figure 3). Such maxima are usually observed in superparamagnetic and spin-glass phases. The empirical Mydosh parameter is helpful in distinguishing between the two behaviors.²¹ The parameter is calculated as $\varphi = (T_{\text{max}}^{\nu_1} - T_{\text{max}}^{\nu_2}) / (T_{\text{max}}^{\nu_1} (\log \nu_1 - \log \nu_2))$, where $T_{\text{max}}^{\nu_i}$ is the temperature of the maximum in the M'' vs T curve at the corresponding frequency. For $\text{LaFe}_{0.2}\text{Co}_{1.8}\text{P}_2$, this parameter was found equal to 0.026(1), which is in the range typical for spin glasses (0.004–0.08).²¹ Calculation of the Mydosh parameter for $\text{LaFe}_{0.1}\text{Co}_{1.9}\text{P}_2$, however, led to inconsistent results. At ac field frequencies of 1000, 100, and 10 GHz, the position of the observed maximum in the M'' vs T dependence almost does not change but at 1 GHz the maximum is shifted to a substantially lower temperature (Figure 3, top).

The observed susceptibility peaks for the samples with $x = 0.1$ and 0.2 can be shifted to lower temperatures by an applied dc magnetic field and finally converted to ferromagnetic-like features (Figure 4). For $\text{LaFe}_{0.1}\text{Co}_{1.9}\text{P}_2$ a field of 0.4 T is required for such conversion, while for $\text{LaFe}_{0.2}\text{Co}_{1.8}\text{P}_2$ a field of 0.01 T results in a similar change.

The magnetic properties of $\text{LaFe}_{0.2}\text{Co}_{1.8}\text{P}_2$ are characteristic of a spin-glass phase, which is easily suppressed by a small magnetic field. The magnetic behavior of $\text{LaFe}_{0.1}\text{Co}_{1.9}\text{P}_2$ appears to be more complicated. To gain further insight into the magnetism of this sample, we investigated its ac susceptibility at a fixed frequency of 1 GHz and applied a dc magnetic field up to 0.1 T, which is not sufficient to fully suppress the observed susceptibility maximum (Figure 4, top). Under such conditions, the appearance of two peaks in the temperature dependence of M' at each nonzero applied field becomes evident (Figure 5).

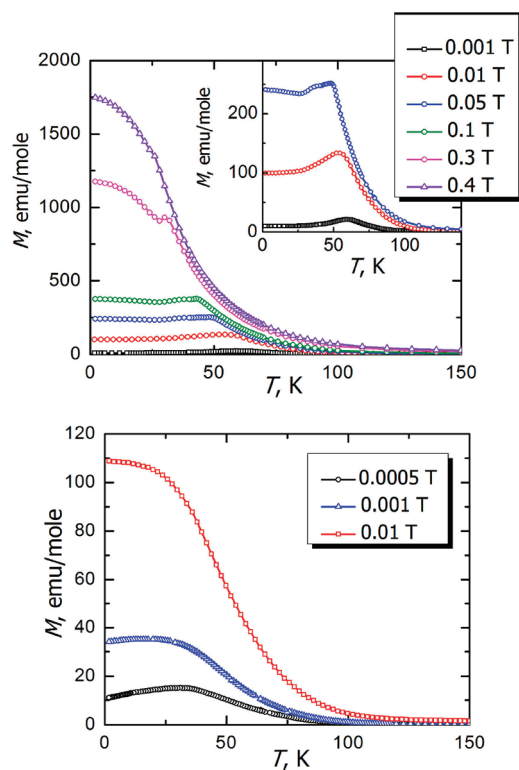


Figure 4. Temperature-dependent magnetization of $\text{LaFe}_{0.1}\text{Co}_{1.9}\text{P}_2$ (top) and $\text{LaFe}_{0.2}\text{Co}_{1.8}\text{P}_2$ (bottom) under different dc bias magnetic fields. (Inset) Enlarged part of the upper plot.

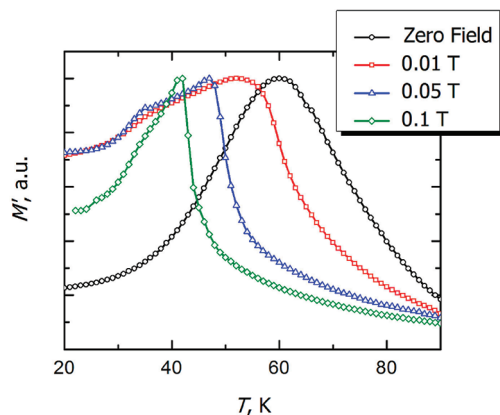


Figure 5. Temperature dependence of ac magnetization of $\text{LaFe}_{0.1}\text{Co}_{1.9}\text{P}_2$ at 1 Hz under different dc bias magnetic fields.

The higher temperature peak, which is essentially frequency independent in zero field, experiences a dramatic shift to lower temperatures with increasing the applied dc field. On the other hand, the shift of the lower temperature peak is much smaller. This behavior, along with the negligible frequency dependence of the higher temperature peak observed in zero field (Figure S2, Supporting Information), may indicate formation of a Griffiths-like phase²² in the range between the two ac magnetization maxima observed for $\text{LaFe}_{0.1}\text{Co}_{1.9}\text{P}_2$. This state is known to emerge in some Ising-type spin glasses²³ and itinerant magnetic semiconductors.²⁴ The Griffiths phase is characterized by the appearance of finite magnetically coupled clusters above the

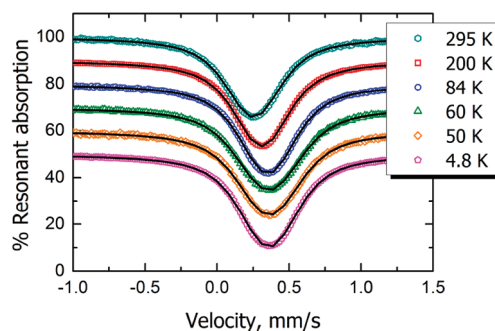


Figure 6. ^{57}Fe Mössbauer spectra of an isotopically enriched sample of $\text{La}^{57}\text{Fe}_{0.1}\text{Co}_{1.9}\text{P}_2$. Black solid lines represent the theoretical fit.

Table 3. Fitting Parameters for ^{57}Fe Mössbauer Spectra of $\text{LaFe}_{0.1}\text{Co}_{1.9}\text{P}_2$

T , K	δ , mm/s	Γ , mm/s ^a
294	0.253(1)	0.192(1)
200	0.310(1)	0.196(1)
84	0.352(1)	0.210(1)
60	0.359(1)	0.287(2)
50	0.362(1)	0.275(2)
4.8	0.360(1)	0.227(1)

^a Full width at half-maximum.

spin-glass transition temperature but below the ordering temperature of the initial ferromagnetically ordered phase (in this case, LaCo_2P_2), although experimental verification of the Griffiths-type transition is not at all straightforward.²⁵ We interpret the observed low-temperature feature as a sign of the spin-glass transition, while the high-temperature feature is attributed to the possible emergence of the Griffiths-like phase. Indeed, one would expect that the latter state should be very sensitive to the applied magnetic field, which increases the probability of percolation of the clustered magnetic structure and establishment of the spin-glass state.

Given the complicated magnetic behavior of $\text{LaFe}_{0.1}\text{Co}_{1.9}\text{P}_2$, we turned to Mössbauer spectroscopy, heat capacity measurements, and neutron diffraction to conclusively establish the absence of magnetic ordering in this compound.

Mössbauer Spectroscopy. Magnetically ordered phases typically exhibit resolved magnetic hyperfine splitting of their Mössbauer spectra below the critical ordering temperature.²⁶ No hyperfine splitting is observed in the ^{57}Fe Mössbauer spectrum of $\text{LaFe}_{0.1}\text{Co}_{1.9}\text{P}_2$ in the temperature range from 294 to 4.8 K (Figure 6), which is in accord with the spin-glass-like behavior of this material. Only one narrow signal is observed, with an isomer shift of 0.25 mm/s, which is close to the isomer shift of Fe in other spin-glass-like intermetallic compounds, e.g., FeAl_2 ²⁷ and $\text{Zn}_{77}\text{Fe}_7\text{Sc}_{16}$.²⁸ The slight increase of the isomer shift upon lowering the temperature is due to the second-order Doppler effect.

In some spin-glass phases, the presence of a weak internal local magnetic field emerging from short-range ordering was shown to result in hyperfine splitting of the Mössbauer spectrum. Depending on the magnitude of the internal field, the hyperfine splitting can either be well resolved,²¹ or appear just as additional broadening of the single-peak spectrum.^{27,29} The latter situation occurs

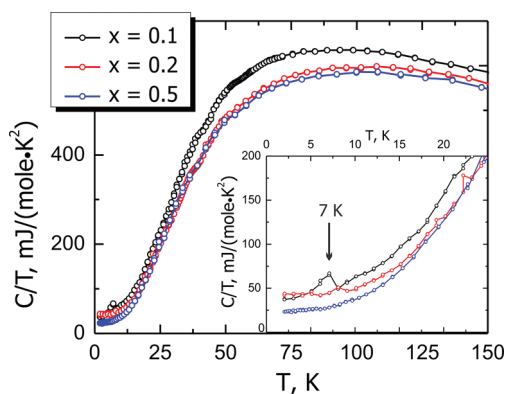


Figure 7. Temperature dependence of the heat capacity for $\text{LaFe}_x\text{Co}_{2-x}\text{P}_2$. (Inset) Low-temperature region.

in $\text{LaFe}_{0.1}\text{Co}_{1.9}\text{P}_2$, for which a significant broadening is observed in 60 and 50 K spectra (Table 3).

Heat Capacity. To investigate the electronic properties of $\text{LaFe}_x\text{Co}_{2-x}\text{P}_2$, the temperature dependence of the heat capacity was measured for the samples with $x = 0.1, 0.2,$ and 0.5 . For all the samples, neither C vs T nor C/T vs T dependence showed any specific features or transitions at $T > 10$ K (Figure 7). Phase transitions associated with long-range magnetic ordering are known to cause a pronounced λ -anomaly in heat capacity at the ordering temperature. The absence of such an anomaly for samples with $x = 0.1$ and 0.2 supports the assumption that these two phases exhibit spin-glass-like behavior.

The heat capacity of a solid is the sum of electronic (C_E) and lattice (C_L) contributions. In the Fermi liquid state, which is a conventional metallic state at low temperatures, C_E is expected to behave as $C_E = \gamma T$, where γ is the Sommerfeld coefficient proportional to $N(E_F)$, the total density of states at the Fermi level: $\gamma = 1/3\pi^2 k_B 2N(E_F)$. Fitting the low-temperature part of the specific heat to the modified Debye law, $C = \gamma T + \beta T^3 + \alpha T^5$, yields the following γ coefficients (in $\text{mJ}/(\text{mol K}^2)$): 34.8(6) ($x = 0.1$), 42(1) ($x = 0.2$), and 23.2(4) ($x = 0.5$) (Figure S2, Supporting Information). This indicates a significant decrease in $N(E_F)$ with increasing Fe content to $x = 0.5$, which is in good agreement with quantum-chemical calculations (see below). For $\text{LaFe}_{0.1}\text{Co}_{1.9}\text{P}_2$, the C/T vs T dependence clearly shows an anomaly at 7 K (Figure 7, inset). No features around this temperature were found in the magnetic studies. Nevertheless, neutron diffraction experiments indicate that some structural distortion occurs at 4 K (see below). We attribute the observed peak in the heat capacity to the structural phase transition associated with this distortion.

Neutron Powder Diffraction. Scattering of neutrons by magnetically ordered spins results in the appearance of new (magnetic) reflections (antiferro- or ferrimagnetic ordering) or intensity enhancement for the existing structural reflections (ferromagnetic ordering) in a powder neutron diffraction (PND) pattern. Thus, the type of magnetic ordering and orientation of Co spins in PrCo_2P_2 and NdCo_2P_2 were unambiguously determined using PND data.³⁰ In contrast, spin-glass phases do not exhibit long-range magnetic ordering, and their PND patterns remain largely unchanged at and below the spin-freezing point, although a weak signal due to short-range ordering may eventually appear as diffuse scattering in the low-angle region.

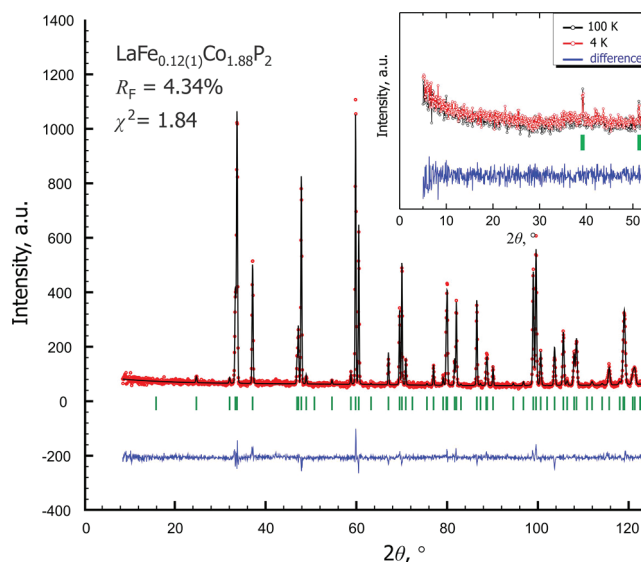


Figure 8. Rietveld refinement (black line) of powder neutron diffraction data (red circles) for $\text{LaFe}_{0.1}\text{Co}_{1.9}\text{P}_2$ collected at 100 K ($\lambda = 1.536$ Å). Green marks indicate theoretical Bragg peak positions. The difference is shown as the blue curve at the bottom. (Inset) Comparison of the low-angle region of PND patterns ($\lambda = 2.41$ Å) collected at 100 (black) and 4 K (red) and the difference curve (blue).

Crystal structure parameters of $\text{LaFe}_{0.1}\text{Co}_{1.9}\text{P}_2$ refined from PND data collected at 100 K are in good agreement with those obtained from room-temperature single-crystal X-ray diffraction. Unlike X-ray diffraction, which cannot distinguish between neighboring Fe and Co atoms, neutron diffraction is ideally suited to make such a distinction due to the large difference in the neutron scattering lengths of Co (2.5 fm) and Fe (9.4 fm). Note that no superstructure formation was observed, which indicates a random distribution of Fe and Co atoms over the transition metal crystallographic site, 4d (0, 1/2, 1/4). Crystal structure refinement resulted in the composition $\text{LaFe}_{0.12(1)}\text{Co}_{1.88(1)}\text{P}_2$, which is close both to the nominal one and to that determined by EDX analysis. A comparison of the PND patterns collected at 100 and 4 K, i.e., at temperatures above and below the susceptibility maximum, reveals neither additional diffraction peaks nor changes in the peak intensities for low-angle reflections (Figure 8, inset). Thus, PND confirms the absence of long-range magnetic ordering in $\text{LaFe}_{0.1}\text{Co}_{1.9}\text{P}_2$. Additionally, some high-angle diffraction peaks exhibit broadening and the appearance of higher angle shoulders at 4 K (Figure 9). We believe that this change is due to a weak structural distortion of $\text{LaFe}_{0.1}\text{Co}_{1.9}\text{P}_2$, which also agrees with the heat capacity data (see above). Experiments to uncover the origin of this structural distortion are currently in progress.

Crystal Structure. The unit cell volume of LaFe_2P_2 ($V = 162.00$ Å³) is slightly larger than that of LaCo_2P_2 ($V = 160.36$ Å³) (Figure 1), as expected from the larger radius of the Fe atom. Room-temperature powder diffraction data refined with an internal standard revealed that the unit cell volume of $\text{LaFe}_x\text{Co}_{2-x}\text{P}_2$ also increases with Fe content, x (Figure 10). Nevertheless, the unit cell parameters a and c exhibit unexpected anomalous changes. The increase in the unit cell volume for higher x is realized via increasing the parameter c , while the parameter a is decreasing (Figure 10), which is opposite to the changes observed when comparing the unit cell parameters of LaCo_2P_2

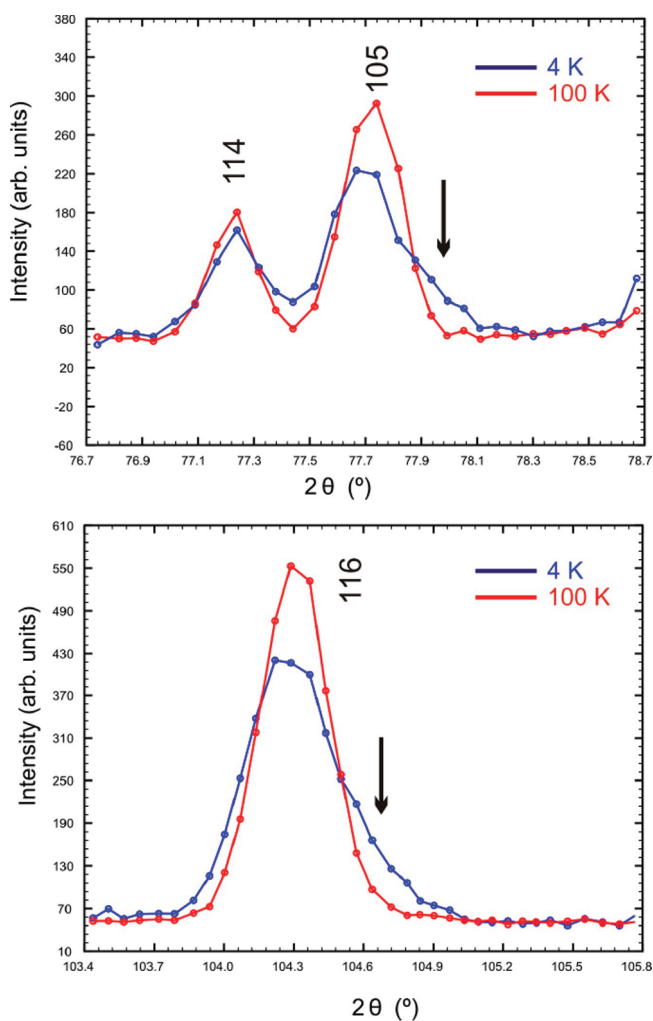


Figure 9. Structural distortion in $\text{LaFe}_{0.1}\text{Co}_{1.9}\text{P}_2$ emphasized by higher angle shoulders appearing for the (105) and (116) powder neutron diffraction peaks at 4 K.

and LaFe_2P_2 . Thus, the solid solutions $\text{LaFe}_x\text{Co}_{2-x}\text{P}_2$ do not follow the simple Vegard behavior.

In the ThCr_2Si_2 structure type, the distance between transition metal atoms within the planar square net is directly proportional to the unit cell parameter a , $d(\text{M}-\text{M}) = a/\sqrt{2}$. Hence, upon introduction of the larger Fe atoms into the Co sublattice of LaCo_2P_2 , the average M–M distance is expected to increase. The X-ray powder diffraction data, however, unambiguously show that the M–M distance in the $\text{LaFe}_x\text{Co}_{2-x}\text{P}_2$ structures decreases with increasing Fe content. Single-crystal X-ray diffraction experiments confirm this observation and also reveal that the average $d(\text{M}-\text{P})$ is almost independent of Fe content, within the esd (estimated standard deviation). These observations suggest that the Fe–Co bonding in these mixed phases is different from the homoatomic Co–Co and Fe–Fe bonding in their ternary congeners. As will be revealed below by quantum-chemical calculations, such a difference has an important influence on the magnetic properties of these materials.

Variable-Temperature Powder X-ray Diffraction. Recently, we have shown that ferromagnetic ordering in $\text{La}_{1-x}\text{Pr}_x\text{Co}_2\text{P}_2$ is associated with an increase in the intralayer Co–Co distance, which is proportional to the unit cell parameter a .³ This is

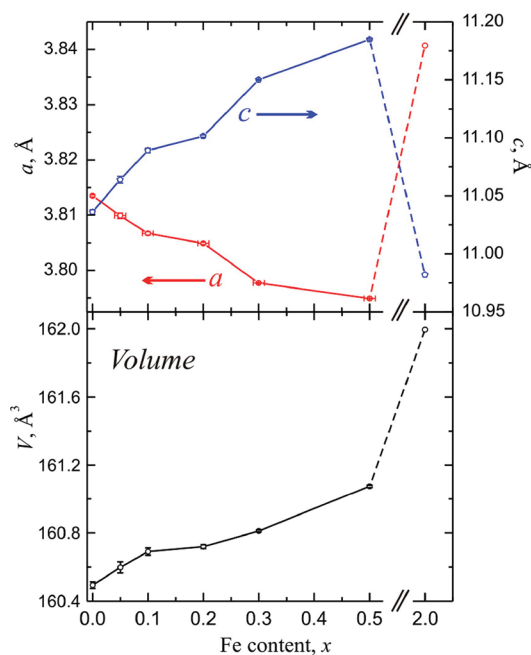


Figure 10. Unit cell parameters and volume of $\text{LaFe}_x\text{Co}_{2-x}\text{P}_2$ as a function of Fe content, x .

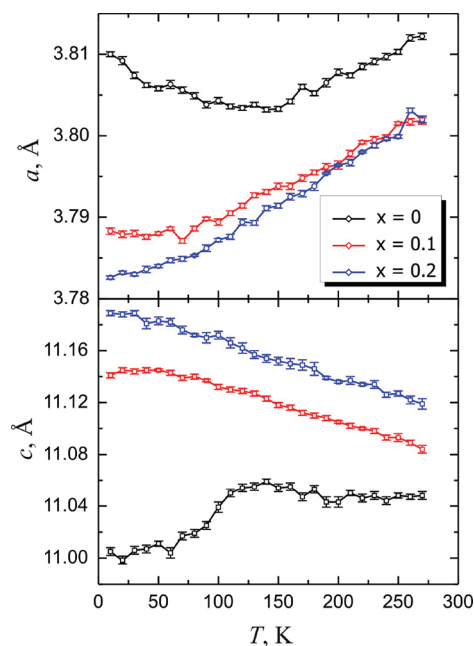


Figure 11. Temperature dependence of unit cell parameters for $\text{LaFe}_x\text{Co}_{2-x}\text{P}_2$ ($x = 0, 0.1, 0.2$).

demonstrated by the temperature dependence of unit cell parameters of LaCo_2P_2 (Figure 11). The parameter a initially decreases with temperature but exhibits an upturn at $T_C = 132$ K. Thus, below T_C the structure expands in the ab plane but contracts along the c axis, which results in the overall reduction of the unit cell volume (Figure S3, Supporting Information). Note that even the smallest parameter c observed ($10.998(4)$ Å at 20 K) is sufficiently large, indicating that the interlayer P–P distance remains above 3 Å and no structural collapse takes place.

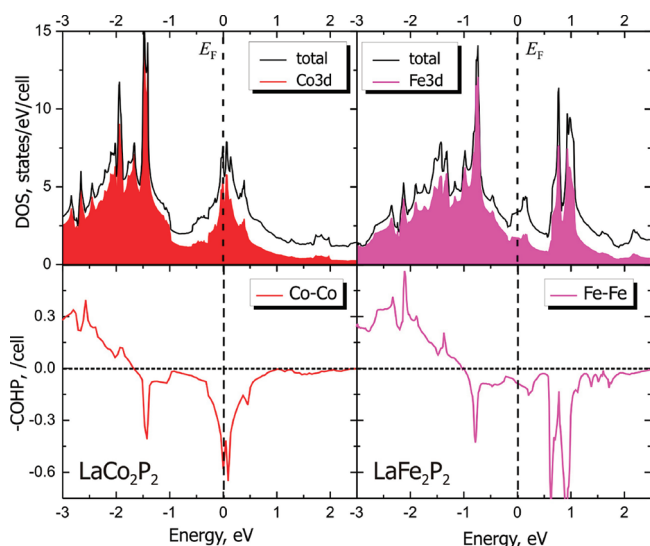


Figure 12. DOS and M–M COHP plots for LaCo_2P_2 (left) and LaFe_2P_2 (right).

In contrast, $\text{LaFe}_{0.2}\text{Co}_{1.8}\text{P}_2$ exhibits no abrupt changes in the temperature dependence of unit cell parameters. The parameter c increases while the parameter a and unit cell volume decrease upon lowering temperature (Figure 11). A similar behavior is observed for $\text{LaFe}_{0.1}\text{Co}_{1.9}\text{P}_2$ above 70 K. Below this temperature, however, the unit cell parameters of $\text{LaFe}_{0.1}\text{Co}_{1.9}\text{P}_2$ remain essentially constant within one esd. Such “freezing” of the unit cell parameters might be associated with the aforementioned formation of the Griffiths phase.

While both LaCo_2P_2 and $\text{LaFe}_x\text{Co}_{2-x}\text{P}_2$ ($x = 0.10, 0.20$) exhibit ferromagnetic nearest-neighbor interactions, as suggested by their positive Curie constants, examination of variable-temperature powder X-ray diffraction patterns indicates a change in the character of M–M bonding upon introduction of Fe into the structure of LaCo_2P_2 . Of course, the Curie constant indicates the sign of magnetic exchange averaged over the entire lattice and does not allow any further judgment about specific interatomic interactions. To get a deeper insight into the nature of magnetic ordering and local M–M bonding in these materials, we turned to quantum-chemical calculations.

Electronic Structure. Nonmagnetic calculations of the electronic band structure of $\text{LaFe}_x\text{Co}_{2-x}\text{P}_2$ ($x = 0, 0.5, 1, \text{ and } 2$) were performed using the LMTO approach.³¹ This method is known to underestimate correlation energies of the 4f states in lanthanides, especially in the case of significant spin–orbit coupling. Nevertheless, it was demonstrated that LMTO produces sufficiently accurate results for the empty f⁰ (La) electronic shell where spin–orbit coupling is not present.³² Therefore, this method is suitable for study of $\text{LaFe}_x\text{Co}_{2-x}\text{P}_2$. First, we compare ternary compounds LaCo_2P_2 and LaFe_2P_2 . The former exhibits ferromagnetic ordering at 132 K, while the latter is paramagnetic in the 1.8–300 K temperature range. The electronic structure of LaCo_2P_2 exhibits a high peak in the electronic density of states (DOS) in the vicinity of the Fermi level (Figure 12, top). On the other hand, for LaFe_2P_2 this peak appears above the Fermi level, because, in the first approximation, substitution of Fe for Co lowers the Fermi energy due to the decrease in the electron count per transition metal atom.

According to the Stoner criterion,³³ an itinerant magnet exhibits ferromagnetism when $I \cdot N(E_F) > 1$, where I is a measure

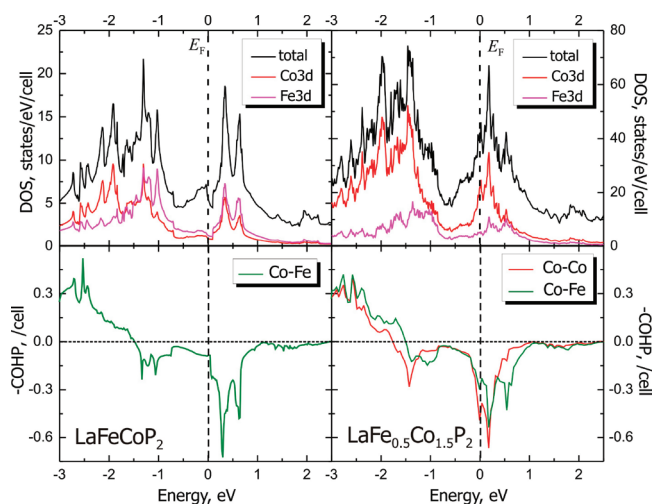


Figure 13. DOS and M–M COHP plots for LaFeCoP_2 (left) and $\text{LaFe}_{0.5}\text{Co}_{1.5}\text{P}_2$ (right).

of the strength of magnetic exchange interaction and $N(E_F)$ is the DOS at the Fermi level. The values of I can be approximated by those known for the elemental metals.^{34,35} From our calculations, the $I \cdot N(E_F)$ product equals 1.6 and 0.8 for LaCo_2P_2 and LaFe_2P_2 , respectively. Thus, the Stoner criterion indicates that LaCo_2P_2 should exhibit ferromagnetic ordering while LaFe_2P_2 should be paramagnetic, which is in agreement with the observed magnetic properties.

For mixed $\text{LaFe}_x\text{Co}_{2-x}\text{P}_2$ compounds, calculations were performed on model ordered superstructures, in which the composition of each transition metal layer was fixed to the corresponding Fe/Co ratio. Thus, only Co–Fe contacts are present within the layer in LaFeCoP_2 , while both Co–Fe and Co–Co contacts are present in $\text{LaFe}_{0.5}\text{Co}_{1.5}\text{P}_2$ (Figure S4, Supporting Information). As expected, in the electronic structure of LaFeCoP_2 the Fermi level is shifted to higher energy relative to the E_F of LaFe_2P_2 but still remains far from the DOS peak in the 3d metal subband (Figure 13, top). In $\text{LaFe}_{0.5}\text{Co}_{1.5}\text{P}_2$, the Fermi level already crosses the DOS peak (Figure 13, top) but the major contribution to this peak at E_F comes from Co 3d orbitals, while the contribution from the Fe 3d orbitals is maximized at energies slightly above E_F . Thus, the DOS calculations clearly demonstrate that increasing the Fe content leads to the lower value of $N(E_F)$,³⁶ which explains, at least qualitatively, the suppression of ferromagnetic ordering in $\text{LaFe}_x\text{Co}_{2-x}\text{P}_2$ with increasing x .

To understand the difference in the local M–M interactions in $\text{LaFe}_x\text{Co}_{2-x}\text{P}_2$, we performed an analysis of crystal orbital Hamiltonian population (COHP). Dronskowski et al. showed that the driving force for ferro- or antiferromagnetic ordering lies in the local nonbonding or antibonding character of states located in the vicinity of the Fermi level.³⁷ While both LaCo_2P_2 and LaFe_2P_2 exhibit antibonding COHP (E_F) along the shortest Co–Co and Fe–Fe distances of ~ 2.7 Å, a strong M–M antibonding peak observed in the former appears far above the Fermi level in the latter (Figure 12, bottom). Thus, we can assume that the presence of a strong M–M antibonding COHP peak at E_F is a prerequisite for magnetic ordering in these materials. Analysis of COHP curves of LaFeCoP_2 and $\text{LaFe}_{0.5}\text{Co}_{1.5}\text{P}_2$ confirms the conclusion drawn earlier from analysis of DOS. In LaFeCoP_2 , a weak M–M antibonding character of COHP is observed (Figure 13, bottom), similar to that of LaFe_2P_2 .

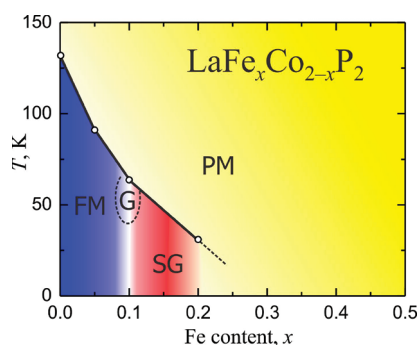


Figure 14. Magnetic phase diagram of $\text{LaFe}_x\text{Co}_{2-x}\text{P}_2$: PM, paramagnet; FM, ferromagnet; SG, spin glass; G, possible Griffiths phase.

Therefore, one should not expect magnetic ordering for this compound. In $\text{LaFe}_{0.5}\text{Co}_{1.5}\text{P}_2$, the Fermi level crosses a strong Co–Co antibonding COHP peak while a Co–Fe antibonding peak lies higher in energy. Thus, substitution of Fe for Co leads not only to the decrease of DOS at E_F but also to the reduction of the antibonding character of M–M interactions. This latter effect, in turn, causes the decrease in the unit cell parameter a and the average intralayer M–M distance with the increase in the Fe content in $\text{LaFe}_x\text{Co}_{2-x}\text{P}_2$ (see the structural discussion above).

CONCLUDING REMARKS

Summarizing the experimental and theoretical results, one can explain the observed changes in the structural and magnetic properties of $\text{LaFe}_x\text{Co}_{2-x}\text{P}_2$ (Figure 14). LaCo_2P_2 exhibits a strong DOS peak at the Fermi level, which leads to ferromagnetic ordering at 132 K. Partial substitution of Fe for Co has two major consequences: (i) The shift of the Fermi level to lower energy results in the reduction of DOS at E_F , which lowers the ordering temperature ($T_C = 91$ K for $\text{LaFe}_{0.05}\text{Co}_{1.95}\text{P}_2$) and eventually suppresses the long-range magnetic ordering for $x \geq 0.10$; (ii) The Co–Fe interaction has a weaker antibonding character as compared to the Co–Co one, indicating that introduction of Fe leads to “dilution” of the magnetic Co substructure. Instead of ferromagnetic ordering, $\text{LaFe}_{0.1}\text{Co}_{1.9}\text{P}_2$ and $\text{LaFe}_{0.2}\text{Co}_{1.8}\text{P}_2$ exhibit spin-glass-like behavior, which can be suppressed by an applied magnetic field. The critical field is much higher for $\text{LaFe}_{0.1}\text{Co}_{1.9}\text{P}_2$ (0.4 T) than for $\text{LaFe}_{0.2}\text{Co}_{1.8}\text{P}_2$ (0.01 T). Note that the increase in the Fe content results in the significant decrease in the saturation magnetization of $\text{LaFe}_x\text{Co}_{2-x}\text{P}_2$ (Figure 3), in good agreement with the theoretical prediction. Increasing the Fe concentration to $x \geq 0.30$ leads to formation of paramagnetic phases.

It is important to mention that the magnetic properties of $\text{CaFe}_x\text{Co}_{2-x}\text{P}_2$ have been studied recently by Cava et al.³⁸ The parent CaCo_2P_2 compound exhibits antiferromagnetic ordering of Co magnetic moments at $T_N = 113$ K.³⁹ Suppression of the magnetically ordered state was observed for $x > 0.2$, which is similar to our findings. No spin-glass properties, however, were reported for $\text{CaFe}_x\text{Co}_{2-x}\text{P}_2$. In this series, a substantial increase in the interlayer P–P distance is observed upon increasing Fe content and the disappearance of antiferromagnetic ordering was attributed to expansion of structure along the c axis. The properties of RCo_2P_2 materials (R = rare-earth metal) are somewhat different. Thus, we have recently shown that for PrCo_2P_2 a significant modification of magnetic behavior can be achieved

while preserving almost the same, relatively short P–P distance (~ 2.57 Å).⁹ The change from antiferromagnetic ordering in PrCo_2P_2 to ferromagnetic ordering in $\text{Pr}_{0.8}\text{Eu}_{0.2}\text{Co}_2\text{P}_2$ and $\text{Pr}_{0.8}\text{Ca}_{0.2}\text{Co}_2\text{P}_2$ was explained by the change in the electronic band structure at the Fermi level, which is expected to have a pronounced influence on the magnetic behavior of itinerant magnets. The series $\text{LaFe}_x\text{Co}_{2-x}\text{P}_2$ reported in this work provides another example of the importance of electronic factors in defining magnetic properties of RCo_2P_2 materials. The change from the ferromagnetic to spin-glass to paramagnetic state has been traced to the difference in the local Fe–Co and Co–Co bonding and the shift in the Fermi level with increasing Fe content. Studies of other possible aliovalent substitutions that can dramatically modify the magnetic behavior of ternary RCo_2P_2 compounds are currently being pursued in our laboratories.

ASSOCIATED CONTENT

S Supporting Information. Additional magnetic and heat capacity plots, details of quantum-chemical calculations. This material is available free of charge via the Internet at <http://pubs.acs.org>.

AUTHOR INFORMATION

Corresponding Author

*E-mail: shatruk@chem.fsu.edu.

Present Addresses

¹Department of Chemistry, University of California at Davis, Davis, CA 95616.

ACKNOWLEDGMENT

This research is supported by the National Science Foundation CAREER Award (DMR-0955353). The experiments at Oak Ridge National Laboratory’s High Flux Isotope Reactor were sponsored by the Scientific User Facilities Division, Office of Basic Energy Sciences, U.S. Department of Energy. We also would like to thank Prof. Ram Seshadri (University of California at Santa Barbara) for helpful discussion of this work. Mössbauer spectra were taken at the NHMFL which is funded by the NSF through the Cooperative Agreement No. DMR-0654118, the State of Florida, and the DOE. The Mössbauer instrument was purchased using the User Collaboration Grant Program UCGP 5064 funds awarded to A.O.

REFERENCES

- (1) Rotter, M.; Pangerl, M.; Tegel, M.; Johrendt, D. *Angew. Chem., Int. Ed.* **2008**, *47*, 7949–7952. Rotter, M.; Tegel, M.; Johrendt, D. *Phys. Rev. Lett.* **2008**, *101*, 107006/1–4.
- (2) Canfield, P. C.; Bud’ko, S. L. *Annu. Rev. Condens. Matter Phys.* **2010**, *1*, 27–50.
- (3) Kovnir, K.; Thompson, C. M.; Zhou, H. D.; Wiebe, C. R.; Shatruk, M. *Chem. Mater.* **2010**, *22*, 1704–1713.
- (4) Jia, S.; Jiramongkolchai, P.; Suchomel, M. R.; Toby, B. H.; Checkelsky, J. G.; Ong, N. P.; Cava, R. J. *Nat. Phys.* **2011**, *7*, 207–210.
- (5) Mörsen, E.; Mosel, B. D.; Müller-Warmuth, W.; Reehuis, M.; Jeitschko, W. *J. Phys. Chem. Solids* **1988**, *49*, 785–795.
- (6) Reehuis, M.; Jeitschko, W. *J. Phys. Chem. Solids* **1990**, *51*, 961–968.
- (7) Chefki, M.; Abd-Elmeguid, M. M.; Micklitz, H.; Huhnt, C.; Schlabit, W.; Reehuis, M.; Jeitschko, W. *Phys. Rev. Lett.* **1998**, *80*, 802–805.

- (8) Jeitschko, W.; Meisen, U.; Möller, M. H.; Reehuis, M. Z. *Anorg. Allg. Chem.* **1985**, *527*, 73–84.
- (9) Kovnir, K.; Reiff, W. M.; Menushenkov, A. P.; Yaroslavtsev, A. A.; Chernikov, R. V.; Shatruk, M. *Chem. Mater.* **2011**, *23*, 3021–3024.
- (10) Akselrud, L. G.; Zavalii, P. Y.; Grin, Y.; Pecharski, V. K.; Baumgartner, B.; Wölfel, E. *Mater. Sci. Forum* **1993**, *133–136*, 335–340.
- (11) *SMART and SAINT*; Bruker AXS Inc.: Madison, WI, 2007.
- (12) Sheldrick, G. M. *Acta Crystallogr., Sect. A* **2008**, *A64*, 112–122.
- (13) Garlea, V. O.; Chakoumakos, B. C.; Moore, S. A.; Taylor, G. B.; Chae, T.; Maples, R. G.; Riedel, R. A.; Lynn, G. W.; Selby, D. L. *Appl. Phys. A: Mater. Sci. Process.* **2010**, *99*, 531–535.
- (14) Jepsen, O.; Burkhardt, A.; Andersen, O. K. *The program TB-LMTO-ASA, Version 4.7*; Max-Planck-Institut für Festkörperforschung: Stuttgart, 1999.
- (15) Von Barth, U.; Hedin, L. *J. Phys. C* **1972**, *5*, 1629–1642.
- (16) Blochl, P. E.; Jepsen, O.; Andersen, O. K. *Phys. Rev. B* **1994**, *49*, 16223–16233.
- (17) Lambrecht, W. R. L.; Andersen, O. K. *Phys. Rev. B* **1986**, *34*, 2439–2449.
- (18) Donohue, P. C. *Mater. Res. Bull.* **1972**, *7*, 943–948.
- (19) Fruchart, R.; Roger, A.; Senateur, J. P. *J. Appl. Phys.* **1969**, *40*, 1250–1257.
- (20) The Curie temperature was determined as an inflection point on the M/H vs T plot.
- (21) Mydosh, J. A. *Spin glasses: an experimental introduction*; Taylor & Francis: Washington, DC, 1993.
- (22) Griffiths, R. B. *Phys. Rev. Lett.* **1969**, *23*, 17–19.
- (23) Randeria, M.; Sethna, J. P.; Palmer, R. G. *Phys. Rev. Lett.* **1985**, *54*, 1321–1324.
- (24) Guo, S.; Young, D. P.; Macaluso, R. T.; Browne, D. A.; Henderson, N. L.; Chan, J. Y.; Henry, L. L.; DiTusa, J. F. *Phys. Rev. Lett.* **2008**, *100*, 017209/1–4.
- (25) Imry, Y. *Phys. Rev. B* **1977**, *15*, 4448–4450.
- (26) In *Mössbauer Spectroscopy Applied to Inorganic Chemistry*; Long, G. J., Grandjean, F., Eds.; Plenum Press: New York, 1984; Vol. 1. (Note, however, that there are important exceptions to this general rule. For example, in the metamagnetic anhydrous FeCl_2 ($T_N = 24$ K) the internal field in zero applied field at 4.2 K is only ~ 0.4 T, owing to the fortuitous cancellation of its primary components, namely, the Fermi contact field (H_F), orbital (H_L), and dipolar (H_D) contributions: Greenwood, N. N.; Gibb, T. C. *Mössbauer Spectroscopy*. Chapman and Hall: London, 1971, p 120.)
- (27) Chi, J.; Li, Y.; Vagizov, F. G.; Goruganti, V.; Ross, J. H., Jr. *Phys. Rev. B* **2005**, *71*, 024431/1–5.
- (28) Al Qadi, K.; Wang, P.; Stadnik, Z. M.; Przewoznik, J. *Phys. Rev. B* **2009**, *79*, 224202/1–15.
- (29) Zaikina, J. V.; Schellenberg, I.; Benbow, E. M.; Pöttgen, R.; Lattner, S. E. *Chem. Mater.* **2011**, *23*, 1768–1778.
- (30) Reehuis, M.; Brown, P. J.; Jeitschko, W.; Möller, M. H.; Vomhof, T. *J. Phys. Chem. Solids* **1993**, *54*, 469–475.
- (31) Andersen, O. K.; Pawłowska, Z.; Jepsen, O. *Phys. Rev. B* **1986**, *34*, 5253–5269.
- (32) Johrendt, D.; Felser, C.; Jepsen, O.; Andersen, O. K.; Mewis, A.; Rouxel, J. *J. Solid State Chem.* **1997**, *130*, 254–265.
- (33) Stoner, E. C. *Proc. R. Soc. London Ser. A* **1938**, *165*, 372–414.
- (34) Janak, J. F. *Phys. Rev. B* **1977**, *16*, 255–262.
- (35) Gourdon, O.; Bud'ko, S. L.; Williams, D.; Miller, G. J. *Inorg. Chem.* **2004**, *43*, 3210–3218.
- (36) The unit cell volume of the hypothetical $\text{LaFe}_{0.5}\text{Co}_{1.5}\text{P}_2$ is 8 times larger than that of LaCo_2P_2 . Therefore, the DOS per one M atom is lower for the former compound.
- (37) Landrum, G. A.; Dronskowski, R. *Angew. Chem., Int. Ed.* **2000**, *39*, 1560–1585.
- (38) Jia, S.; Chi, S.; Lynn, J. W.; Cava, R. J. *Phys. Rev. B* **2010**, *81*, 214446/1–7.
- (39) Reehuis, M.; Jeitschko, W.; Kotzyba, G.; Zimmer, B.; Hu, X. *J. Alloys Compd.* **1998**, *266*, 54–60.